Computational Materials Science 197 (2021) 110646

Contents lists available at ScienceDirect

Computational Materials Science

journal homepage: www.elsevier.com/locate/commatsci

Atomistic and continuum modeling of 3D graphene honeycombs under uniaxial in-plane compression

Yiqing Chen [a], Fanchao Meng [b,*], Xiaohan Bie [a], Pengfei Ou [a,c], Jun Song [a,*]

[a] Department of Mining and Materials Engineering, McGill University, Montreal H3A 0C5, Canada
[b] Institute for Advanced Studies in Precision Materials, Yantai University, Yantai, Shandong 264005, China
[c] Department of Electrical and Computer Engineering, University of Toronto, 35 St. George Street, Toronto, ON M5S 1A4, Canada

ARTICLE INFO

Keywords:
3D graphene honeycombs
Analytical modeling
Structure–property relationships
Carbon allotrope

ABSTRACT

Using large-scale molecular dynamics (MD) simulations in conjunction with continuum modeling, the deformation behaviors of three-dimensional (3D) graphene honeycomb structures under uniaxial in-plane compression have been systematically investigated. The stress-strain responses of graphene honeycombs were found to be dependent on the loading direction, prism size and lattice orientation, but little affected by the junction type. Two critical deformation events, i.e., elastic buckling and structural collapse, were identified, with the associated local and global structural changes associated at these critical events clarified. Continuum models accounting for the effect of lattice orientation and size-dependent yielding have been developed to quantitatively predict the threshold stresses for those critical deformation events. In addition, it has been demonstrated that the overall stress-strain curve of graphene honeycomb can also be reasonably well predicted via continuum modeling, *albeit* deviation at large strains due to effect of junction on cell wall bending. The present study provides critical mechanistic understanding and predictive tools for optimizing and designing 3D graphene honeycombs in small-scale applications.

1. Introduction

Graphene is a two-dimensional (2D) material comprised by an atomically-thin layer of sp^2-bonded carbon atoms in a hexagonal lattice. Thanks to its unique structure, graphene possesses remarkable properties including high electronic quality, large specific surface area, superior thermal conductivity, outstanding mechanical properties, etc. [1–4]. These extraordinary properties have been widely employed for novel applications in many areas, such as electronics, sensors, energy storage and nanocomposites [5]. However, the 2D structural signature of graphene is also a curse, bringing many limitations. For example, graphene usually suffered from ultra-low bending rigidity, leading to low mechanical stability in the out-of-plane direction [6,7]; the corrugations such as wrinkles and ripples in graphene further decrease its shear strength [8]. Moreover, aggregation and restacking of graphene nanosheet often occur during its fabrication due to the strong van der Waals interaction, resulting in poor stability of the fabricated graphene compared with its bulk counterpart [9,10]. Thus, to further realize the full potential of graphene in practical device applications, it is necessary to engineer the structure of graphene.

Several strategies have been proposed to mediate the above negative impact while keeping the advantages of graphene. For instance, graphene-nanoparticle hybrids have been reported to prevent the aggregation of graphene layers, where nanoparticles can increase the interlayer spacing by functioning as a “spacer”, thereby ensuring the high specific surface area and possessing beneficial functionalities for biosensors and catalysts [11,12]; ultraflat graphene layers have been produced by depositing graphene onto atomically flat substrates such as mica to suppress or remove the intrinsic winkles, promising a possible route towards the design and fabrication of wrinkle-free graphene based devices[13,14]; the assembly of graphene into three-dimensional (3D) networks has been shown to inherit the strong mechanical properties of graphene, while meanwhile can prevent graphene sheet aggregation and enable good mass transport [15,16].

Among those afore-mentioned strategies, direct transforming graphene into a 3D graphene structure is particularly attractive. Comparing with other approaches, this approach, a 2D-3D scale-up of graphene, has been demonstrated to be experimentally feasible and controllable [17–19]. The resultant 3D architecture also is also much easier to handle and manipulate than its 2D constituents [20], a great benefit for

* Corresponding authors.
E-mail addresses: mengfanchao@ytu.edu.cn (F. Meng), jun.song2@mcgill.ca (J. Song).

https://doi.org/10.1016/j.commatsci.2021.110646
Received 12 April 2021; Received in revised form 3 June 2021; Accepted 4 June 2021
Available online 15 June 2021

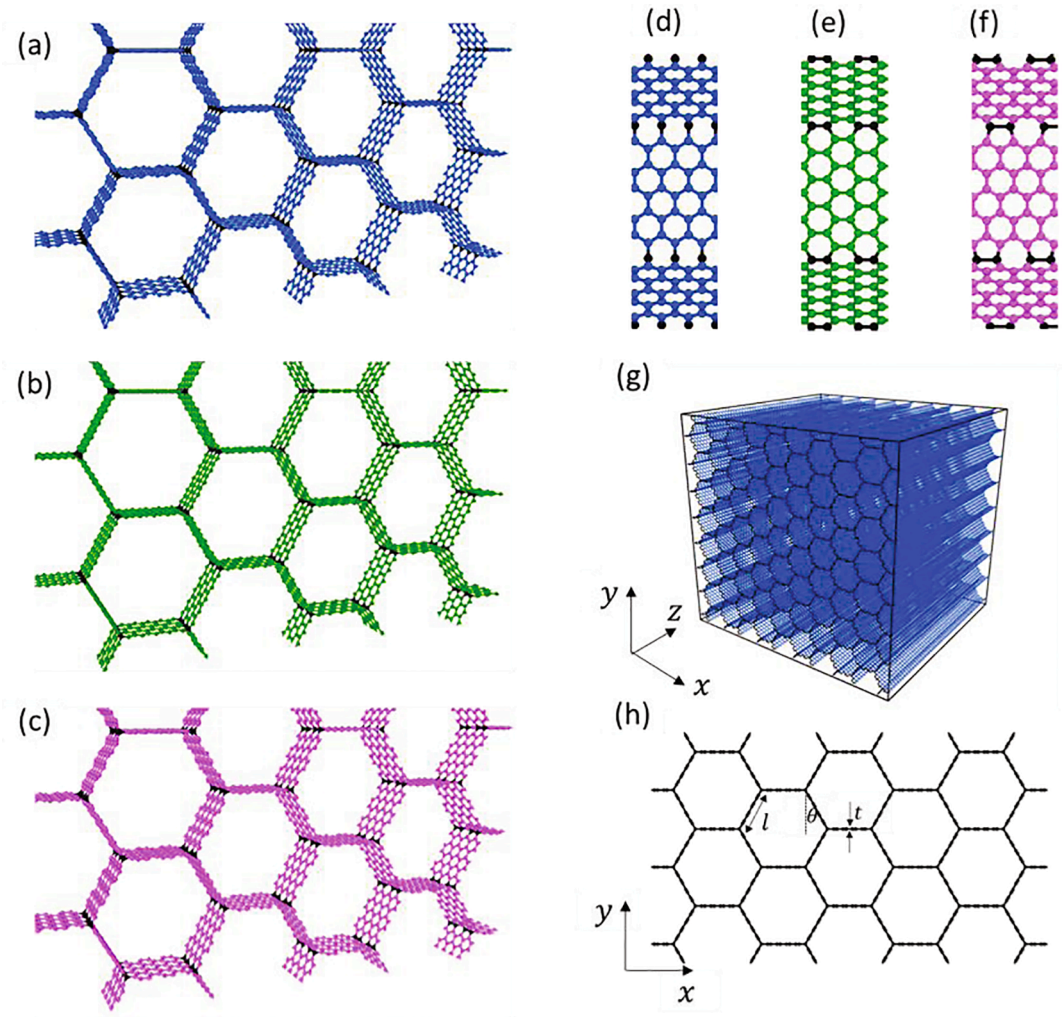

Fig. 1. 3D graphene honeycomb structures considered in this study, illustrated using $ac_6-sp^2sp^2$, $zz_5-sp^2sp^3$ and $ac_6-sp^2sp^3$ as representatives in (a-c) under prospective views and (d-f) under top views. Sample simulation supercell is shown in (g), where atoms colored in black are for easy visualization. In our simulations, 3D graphene honeycombs are compressed along x or y axis, as illustrated in (h), where the length of the honeycomb prism, angle and thickness are denoted as l, θ and t, respectively.

practical applications. One realization of such 2D-3D scale-up is to covalently bond 2D graphene sheets into a 3D honeycomb structure with hexagonal crystal symmetry, which was first hypothesized by Karfunkel and Dressler in 1992 [21]. Recently, this 3D honeycomb structure has been fabricated experimentally by Krainyukova and Zubarev [17], and has been demonstrated to exhibit remarkable stability and high levels of physical adsorption. Additional studies that follow have further discovered and demonstrated various unique properties of 3D graphene honeycomb structures, including theoretically high thermal conductivity [22,23], high lithium storage capability [24] and giant energy absorption capability [25], among others.

Macroscopically honeycomb-type structures have found wide use in structural applications [26,27]. This, in turn, has motivated considerable efforts in investigating the mechanical properties and deformation behaviors of 3D graphene honeycombs and their derivatives. Pang et al. performed tensile loading along the in-plane and out-of-plane directions of 3D graphene honeycomb structure and demonstrated a specific high strength tunable by the cell size [23]. Zhang et al. studied graphene honeycombs under in-plane compression along the zigzag direction, illustrating a self-localized deformation in honeycomb lattice and revealing an important relationship between the mechanical properties and honeycomb cell size [28]. Meng et al. investigated the out-of-plane compressive behaviors of 3D graphene honeycombs using a set of continuum models, which accurately predict the threshold stress at critical deformation events [29]. The afore-mentioned studies have demonstrated the unique mechanical properties of 3D graphene honeycombs and provided valuable knowledge regarding the responses of 3D graphene honeycombs under different loading conditions. However, despite those great prior efforts, one aspect that remains not well understood is the mechanical response of 3D graphene honeycombs under in-plane compression, for which the deformation mechanisms involved remain elusive, with quantitative and predictive description of deformation behaviors missing. In addition, the key atomic characteristics affecting the deformation of 3D graphene honeycombs have not been identified and clarified.

In light of the above limitations, this work systematically studied the deformation behaviors of 3D graphene honeycomb structures under in-plane compression, employing large-scale atomistic simulations in combination with continuum modeling. Graphene honeycombs of different ribbon orientations and atomic bonding at the cell junction were constructed and examined, with the critical deformation events identified. Analytical models that can quantitatively capture those critical events were developed to offer mechanistic insights into the in-plane deformation behaviors of the graphene honeycomb. The present study offers comprehensive understanding of the in-plane deformation behaviors of 3D graphene honeycombs and can be extended to study

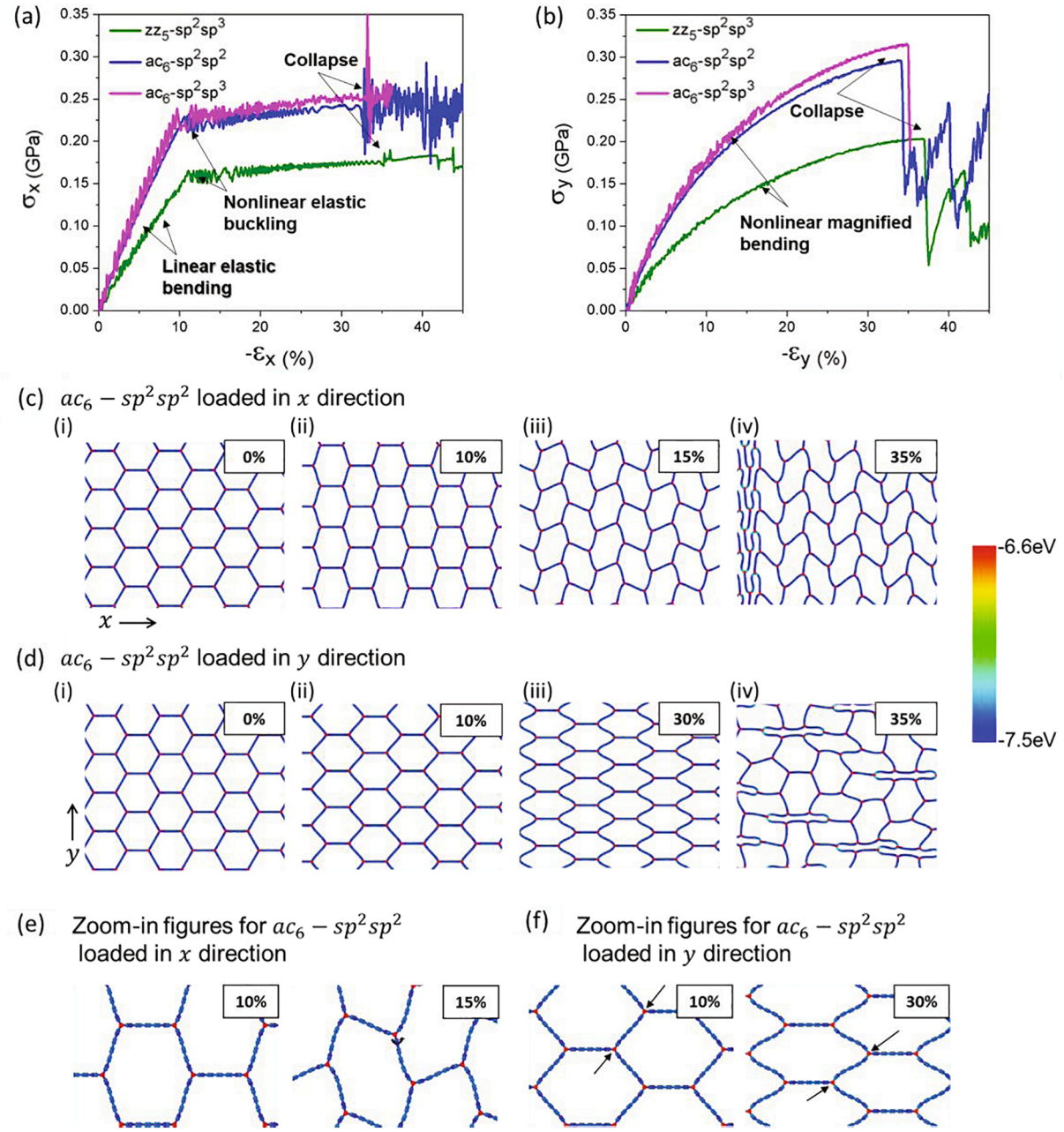

Fig. 2. Representative stress–strain curves of $zz_5-sp^2sp^3$, $ac_6-sp^2sp^2$, and $ac_6-sp^2sp^3$ honeycombs uniaxially compressed along (a) x and (b) y directions, with the critical deformation or fracture events marked next to the corresponding curves. (c) and (d) are the front projection views for $ac_6-sp^2sp^2$ honeycomb loaded in x and y directions, respectively. (e) and (f) show the zoom-in figures for $ac_6-sp^2sp^2$ honeycombs loaded in x and y directions at 10% and 15% or 30% strain respectively, with the junction rotation and non-co-linear axial load on the bond depicted between black arrows. In (c)-(f), atoms are colored according to their potential energies.

other 2D nanomaterial-based 3D honeycomb structures.

2. Computational method

Three types of 3D graphene honeycomb structures were considered in this study as shown in Fig. 1a-c in prospective views and Fig. 1d-f in top views. These honeycombs were named according to the orientation of graphene ribbons that constitute the cell wall, followed by sequentially atomic bonding types at the wall and at the junction, with this name conversion adopted from previous studies [29,30]. For example, the honeycombs in Fig. 1a,d are constituted by armchair (AC) oriented ribbons with sp^2-bonded carbon atoms in both walls and junctions, thus denoted as $ac_n-sp^2sp^2$. Similarly, the honeycombs constituted by zigzag (ZZ) ribbons in Fig. 1b,e and Fig. 1c,f were named as $zz_n-sp^2sp^3$ and $ac_n-sp^2sp^3$ respectively. The subscript n in these notations indicates the number of hexagons between the two junction lines. Among those structures examined, it is worth noting that the $ac_n-sp^2sp^2$ and $ac_n-sp^2sp^3$ honeycombs have been fabricated experimentally and shown to be stable in simulations [17,23,29,31]. Meanwhile, the $zz_n-sp^2sp^3$honeycomb group has been theoretically confirmed to be stable configurations, though not reported experimentally [30–32]. In addition, in the present study we only consider graphene honeycombs consisting of equilateral honeycomb prisms, i.e., $\theta = 30^\circ$ for all honeycombs (see Fig. 1h), as honeycomb structures of random pore/prism sizes have been shown to exhibit poor scalability and uncontrollable porous distribution [33,34].

Table 1
Threshold stress and strain values corresponding to critical events, i.e., elastic buckling and structural collapse, for three representative honeycombs, $ac_6-sp^2sp^2$, $ac_6-sp^2sp^3$ and $zz_5-sp^2sp^3$, under loading along x or y direction.

		Elastic buckling	Structural collapse		
Honeycomb	Loading direction	Stress (GPa)	Strain (%)	Stress (GPa)	Strain (%)
$ac_6-sp^2sp^2$	x	0.229	10.6	0.238	32.7
	y	–	–	0.296	33.9
$ac_6-sp^2sp^3$	x	0.239	9.6	0.247	33.1
	y	–	–	0.313	35.0
$zz_5-sp^2sp^3$	x	0.165	12.4	0.179	35.2
	y	–	–	0.203	36.9

The deformation behaviors of 3D graphene honeycombs were examined through large-scale molecular dynamics (MD) simulations, performed using the (Large-scale Atomic/Molecular Massively Parallel Simulator) LAMMPS package [35]. The interatomic interactions within the material are described by the adaptive intermolecular reactive empirical bond order (AIREBO) potential [36], with the smaller cut-off distance in the switching function modified from 1.7 Å to 2.0 Å to avoid the non-physical post-hardening behavior [37–39]. In the simulation, a rectangular supercell containing the graphene honeycomb was constructed, as shown in Fig. 1g. The in-plane dimension of the simulation supercells ranges from 115 Å by 107 Å (89,600 atoms) to 398 Å by 368 Å (331,520 atoms) for the $ac_n-sp^2sp^2$ and $ac_n-sp^2sp^3$ honeycombs, and 109 Å by 101 Å (84,320 atoms) to 327 Å by 302 Å (262,880 atoms) for the $zz_n-sp^2sp^3$ honeycombs, while the out-of-plane dimension (i.e., z dimension) is kept as around 135 Å for the $ac_n-sp^2sp^2$ and $ac_n-sp^2sp^3$ honeycombs and 130 Å for the $zz_n-sp^2sp^3$ honeycombs. The supercell dimensions were chosen to accommodate honeycomb cells of different prism length l, and also to ensure no size dependence of the simulations results, i.e., for a honeycomb with a specific l, the results were confirmed to remain unchanged with further enlargement of the supercell size.

Periodic boundary conditions were applied in all three directions. During the simulations, all honeycomb models were first relaxed with the isothermal-isobaric (NPT) ensemble at temperature of 1 K for 100 picoseconds (ps) to reach equilibrium. Following this initial relaxation,

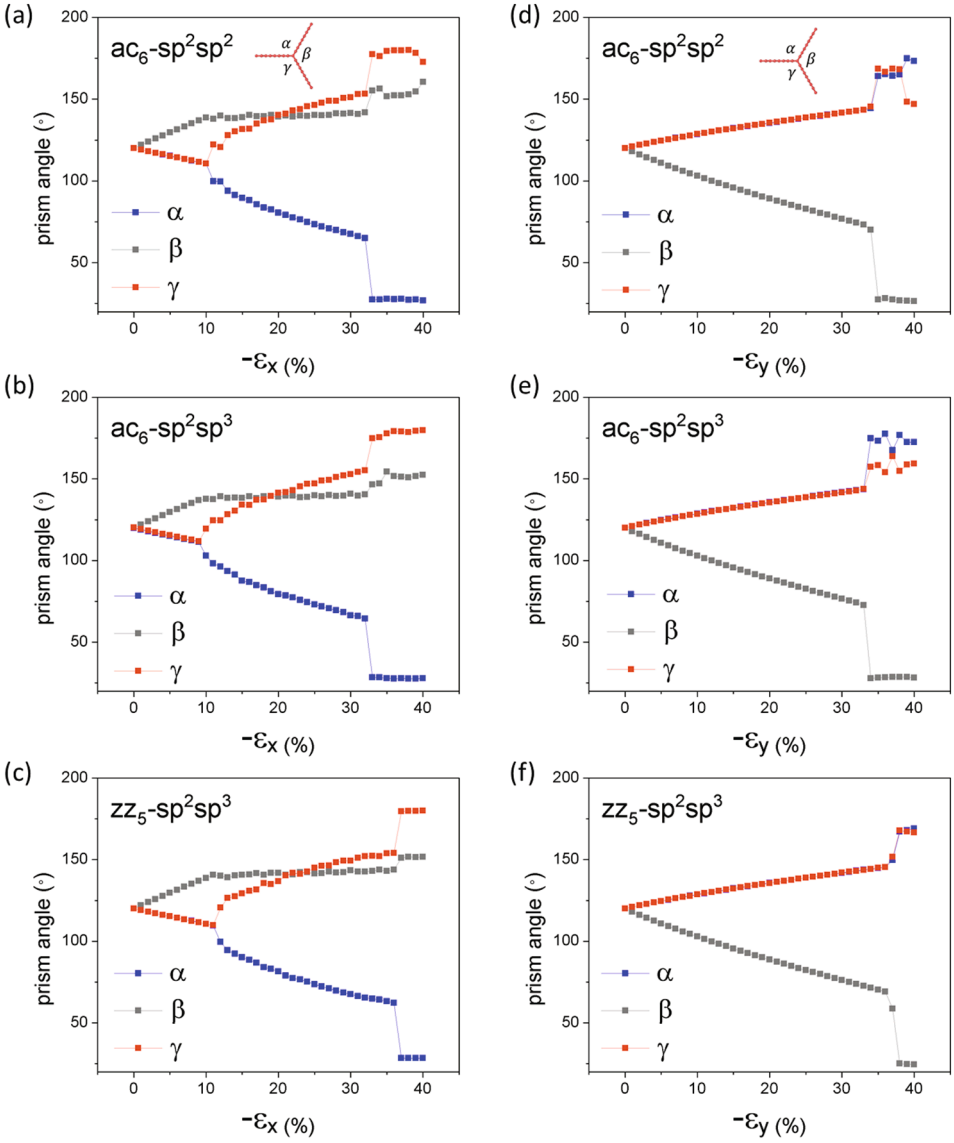

Fig. 3. Prism angle as functions of strain for $ac_6-sp^2sp^2$, $ac_6-sp^2sp^3$ and $zz_5-sp^2sp^3$ honeycombs under loading in (a-c) x direction and (d-f) y direction. Two abrupt changes in slope can be observed in (a)-(c), corresponding to the onset of elastic buckling and structural collapse, while one obvious change can be obtained in (d)-(e) representing the structural collapse.

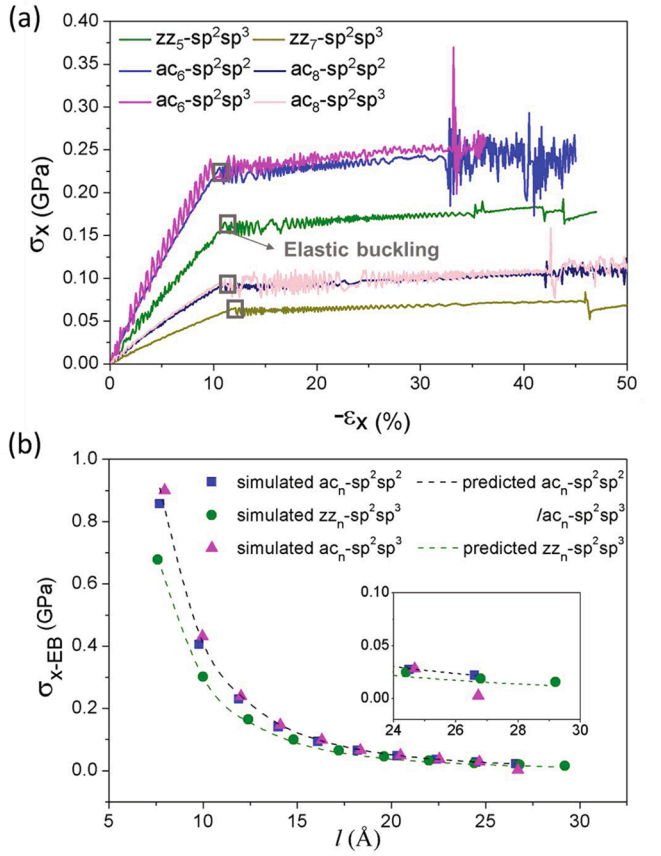

Fig. 4. (a) Representative stress–strain curves from the in-plane compression loaded along the x direction for $ac_6-sp^2sp^2$, $zz_5-sp^2sp^3$ and $ac_6-sp^2sp^3$ honeycombs with different prism length l. (b) Simulated and predicted (i.e., Eq. (1)) critical buckling stress σ_{x-EB} versus l curves for $ac_6-sp^2sp^2$, $zz_5-sp^2sp^3$ and $ac_6-sp^2sp^3$ honeycombs, with the inserted figure showing the convergence of σ_{x-EB} data at large l values.

the system is then loaded under uniaxial compression along one in-plane direction (i.e., x or y direction, cf. Fig. 1g), at a strain rate of $10^{-4}ps^{-1}$ until failure, with the deformation process and structural evolution monitored and analyzed. The timestep of 1 fs (fs) was used for all simulations.

3. Results and discussion

3.1. Stress–strain response of 3D graphene honeycomb structures

Fig. 2a and 2b show the stress–strain curves of three representative honeycombs loaded in x and y directions respectively. For the purpose of comparison, these honeycombs shown correspond to the three different types of honeycombs of similar prism length l, i.e., $ac_6-sp^2sp^2$ ($l = 11.9$Å), $zz_5-sp^2sp^3$ ($l = 12.4$Å) and $ac_6-sp^2sp^3$ ($l = 12.1$Å). As seen in Fig. 2, the stress–strain response exhibits distinct characteristics when a honeycomb is compressed along different directions, but rather insensitive to the different bonding characteristics (at the junction or in the honeycomb wall) of honeycombs. Such similarity in the stress–strain response is also reflected in the structural evolution, with the same set of critical deformation/failure events observed for different honeycombs. As such, we use $ac_6-sp^2sp^2$ honeycomb as a representative in illustrating the structural evolution events during compression along x and y, shown in Fig. 2c and 2d respectively. Particularly for compression along x direction (cf. Fig. 2a), at small strain, the honeycomb deforms via linear elastic bending (e.g., Fig. 2c.i), and in accordance, the stress–strain curve exhibits an initial linear region. As the strain increases beyond ~ 10%, elastic buckling occurs (e.g., Fig. 2c.ii), accompanying which the curve endures a sharp decrease in its slope to become nearly flat. Further loading post this threshold event leads to continuously increasing magnitude of buckling (e.g., Fig. 2c.iii) until structural collapse (Fig. 2c.iv). On the other hand, for compression in y direction (c.f. Fig. 2b), the stress–strain curve stays nonlinear from the very beginning. The stress monotonically increases with the strain in a smooth fashion, until the eventual structural collapse at which clear, abrupt drops in stress are observed (c.f. Fig. 2b). Also as illustrated in Fig. 2d, for deformation under compression along y, the overall structure does not exhibit apparent structural instability before the eventual failure.

The threshold stresses and strains corresponding to those critical events (i.e., elastic buckling and structural collapse) for the three honeycomb groups are listed in Table 1. It is interesting to note from Table 1 that, for the same honeycomb, the threshold stress and strain values corresponding to structural collapse are relatively insensitive to the direction of loading, with the ones associated with y direction compression being slightly higher.

Further elaborating on the structural evolution during deformation, for compression along x direction (cf. Fig. 2c), we note that the structure undergoes transition from the initial elastic bending to elastic buckling at ~ 10% strain, indicated by the junctions of honeycomb cells starting to rotate. In particular, we can see that neighboring junctions rotate in the opposite direction, which is similar to the "anti-rolls" deformation mode [40] . The atomic configurations before and after elastic buckling are also better illustrated in the zoom-in figures shown in Fig. 2e. Loading beyond the occurrence of elastic buckling leads to increased magnitude of buckling until eventual structural collapse which occurs at the localized bands along the ZZ direction in an asymmetric shearing mode of deformation (cf. Fig. 2c.iv). This mode of structural collapse is in agreement with the previous work conducted by Zhang et al. [28]. Under further deformation, the collapse then extends to neighboring columns of honeycomb cells, and continues till all cells are compacted. Also it is worthy to note that overall the collapse consists of multiple discrete events (with each event corresponding to compacting of one or several columns of cells), with each resulting in an abrupt fluctuation in the stress–strain curve (see Fig. 2a). The above observations, despite 3D graphene honeycomb being nanoscopic, are in good agreement with the continuum prediction of the failure characteristics of macroscopic honeycomb under uniaxial loading [26].

Meanwhile, for compression along y direction (cf. Fig. 2d), no obvious junction rotation was observed during the deformation before the eventual structural collapse. This difference (as compared to the case of compression along x) can be attributed to the symmetry of the honeycomb structure (see Fig. 2d), and the loading states resulted from that, as pointed out by Zhu and Mills [41]. The non-linearity in the stress - strain curve is likely caused by the switching from the co-linear to non-co-linear axial load on the bonds (see Fig. 2f), which magnifies the moment and deflection by a factor of $1/(1-P_a/P_{crit})$, where P_a is the axial component of the load and P_{crit} is the Euler load, as suggested by Gibson and Ashby. [26]. In addition, the reason why nonlinear bending is only present for loading in the y axis can be attributed to the higher axial load when loaded in the y axis (i.e., $\sqrt{3}\sigma_y$) than that loaded in the x axis (i.e., $\sigma_x/2$). Moreover, structural collapse under loading in the y direction begins with sudden bond flattening at junction nodes to cause individual cell compaction, with the affected cells randomly distributed throughout the lattice, leading to abrupt fall in the stress–strain response followed by an upturn, as larger load is needed to further the collapse in other cells. As shown in Fig. 2d.iv, the deformation develops a so-called "rectangles" mode under compression along y axis [40]. It is worth noting that a previous study on 3D graphene honeycombs captures a shear band behavior when the honeycomb is subjected to compression in y direction [42]. Such different responses to compression in y direction arise from the different prism size used in simulations (7.6–29.2 Å in

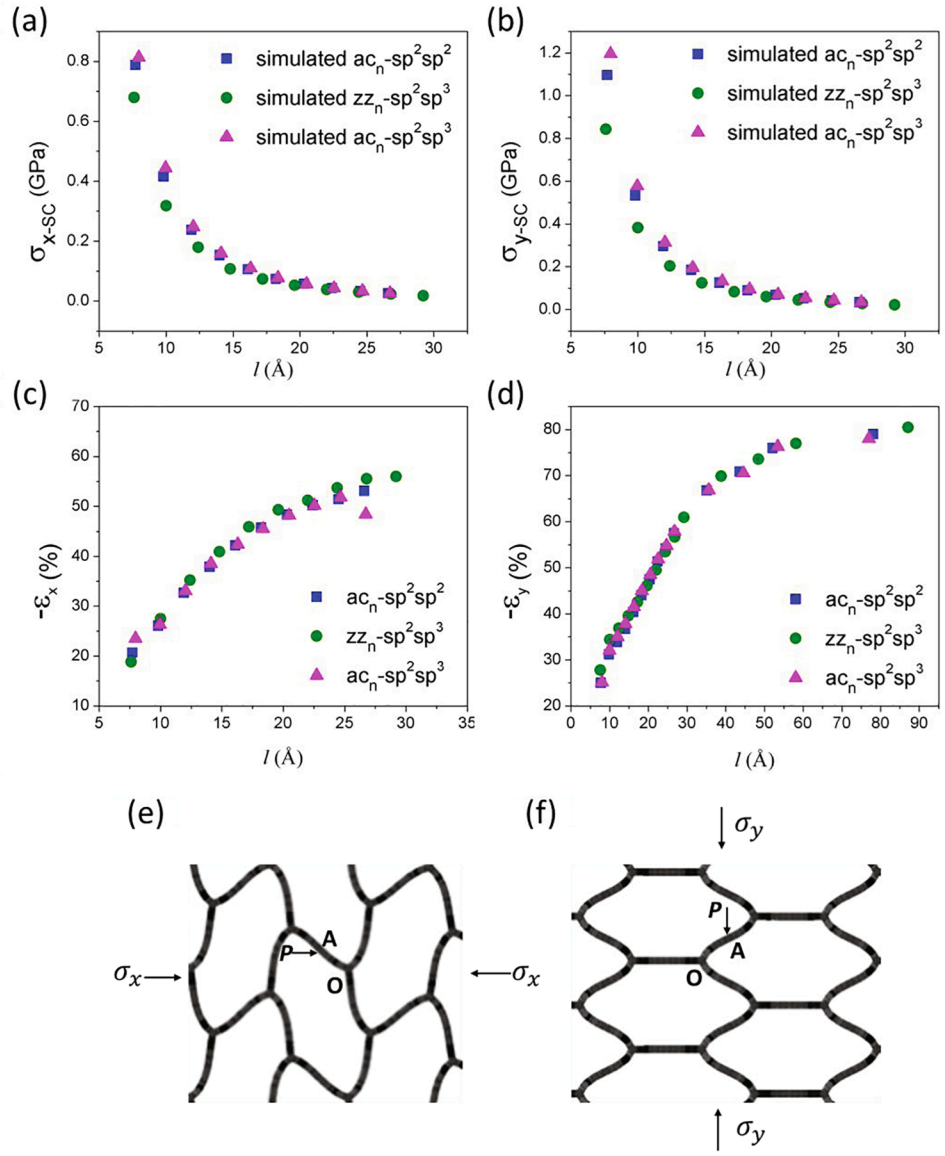

Fig. 5. Simulated and predicted critical structural collapse stress σ_{x-SC} and σ_{y-SC} *vs.* l curves for $ac_6-sp^2sp^2$, $zz_5-sp^2sp^3$ and $ac_6-sp^2sp^3$ honeycombs under loading along (a) x and (b) y directions respectively. (c) and (d) show the dependence of the critical collapse strain on prism length l loaded along x and y directions, respectively. (e) and (f) are schematics for honeycombs compressed at high strains under loading along x and y directions respectively, and the deformed half honeycomb cell wall OA can be seen as a cantilever beam fixed at junction O and loaded at point A by a force P.

our simulation, while 57.6 Å in Ref. [42]). As a consequence of the small prism size used in our study, the random collapse of individual cells happens before the occurrence of shear bands.

As described above, the deformation process involves bond rotation or bending. As such, the critical events during deformation may be also tracked by monitoring the evolution of honeycomb prism angles (α, β and γ) as functions of the compressive strain (ε_x or ε_y), as shown in Fig. 3. We can see that the abrupt changes in value or slope of the prism angle *vs.* strain plot well correspond to the critical events of elastic buckling and eventual structural collapse. Besides, the curves for three honeycombs show rather similar trends for both loading directions, which again demonstrates that the characteristics of the deformation are insensitive to the types of the cell junctions and the orientations of graphene nanoribbons that constitute the honeycomb walls.

In the following sections, those critical events identified are further analyzed with their dependence on the honeycomb prism length l elucidated and predictive models developed.

3.2. Elastic buckling

As afore-discussed, elastic buckling only occurs during loading along x direction. In Fig. 4a, representative stress–strain responses of $ac_n-sp^2sp^2$, $zz_n-sp^2sp^3$ and $ac_n-sp^2sp^3$ honeycombs with different honeycomb prism length l loaded along x direction are plotted. We see from Fig. 4a that the critical buckling strain for the three types of honeycombs are all in the vicinity of 10%, which is in excellent agreement with Euler buckling theory and the results in the previous study by Zhang et al. [26,31]. Based on those stress–strain curves, the critical buckling stress (see Fig. 4a), σ_{x-EB}, can be obtained, and is plotted as a function of l in Fig. 4b. It can be seen that σ_{x-EB} decreases monotonically as l increases. At large values of l, we see that σ_{x-EB} data from different lattice structures converge to a single curve. This suggests that for the threshold elastic buckling stress is not dependent on the lattice structure when the honeycomb cell is sufficiently large. In addition, the σ_{x-EB} *vs* l data of $ac_n-sp^2sp^2$ and $ac_n-sp^2sp^3$ mostly overlap with each other, indicative of the threshold buckling being determined by the orientation of the ribbon instead of the type of the atomic bonding at the junction. Furthermore, overall the AC honeycombs exhibit larger σ_{x-EB} than that of ZZ honeycombs of the same prism size, with the difference being more notable at small values of l. Such difference can be attributed to the fact of the AC nanoribbon having a stronger resistance to deformation than the ZZ nanoribbon [39,43].

From the previous work by Gibson and Ashby [26], a continuum

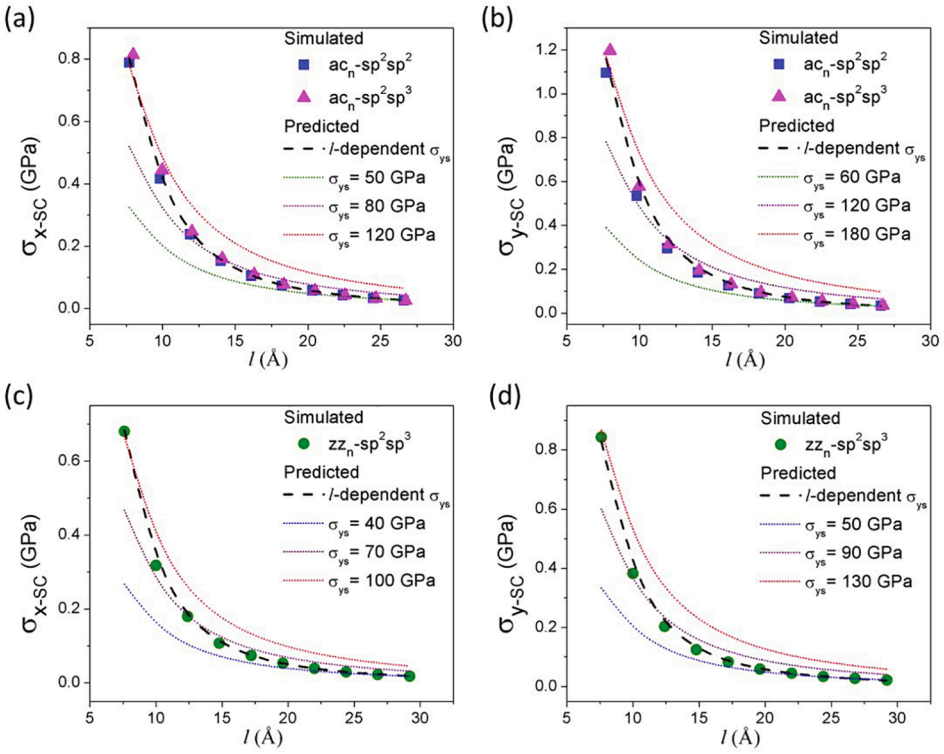

Fig. 6. Predicted critical structural collapse stress σ_{x-SC} or σ_{y-SC} *vs.* l curves for (a)-(b) AC or (c)-(d) ZZ honeycombs using l-dependent σ_{ys} and various constant σ_{ys}.

model has been established for a homogenous honeycomb-type cellular solid, where the threshold elastic buckling stress may be predicted as $E_s\frac{n^2\pi^2}{24}\frac{t^3}{l^3}\frac{1}{\cos\theta}$, where , θ, t and l are the Young's modulus of the solid cell wall material, honeycomb prism angle, thickness of the wall, and honeycomb prism length respectively, while n is an end constraint factor that describes the rotational stiffness of the junction. However, this model does not account for the different lattice structure of the honeycomb cell wall. In this regard, we have modified the original model as:

$$\sigma_{x-EB} = pE_s\frac{n^2\pi^2}{24}\frac{t^3}{l^3}\frac{1}{\cos\theta} \tag{1}$$

where a prefactor p is introduced to incorporate the effect of the lattice structure. For the graphene honeycomb, the modulus $E_s = 1TPa$ and the prism angle $\theta = \pi/6$, while the wall thickness is taken as $t = 0.76$Å according to previous studies [29,44]). The end constraint factor n is set as 0.686 for equilateral honeycomb prisms [26]. Fitting Eq. (1) to the simulated critical buckling stress *vs.* l data in Fig. 4b, we can determine the values of p to be 4.2 and 3.1 for AC and ZZ graphene honeycombs respectively. The larger p value for AC honeycombs indicates their generally better resistance against elastic bulking than the ZZ honeycombs. Such difference in p value can be attributed to more carbon atoms in graphene nanoribbons along the direction perpendicular to the junction line for an AC honeycomb than that for a ZZ honeycomb of the same l. From Fig. 4b, we see that the prediction $\sigma_{x-EB}$from Eq. (1) exhibits excellent agreements with the simulation data.

3.3. Structural collapse

Now we focus on the other category of critical deformation events, i.e., structural collapse of the honeycomb. Unlike elastic buckling which exclusively occurs for the x direction, structural collapse occurs for both x and y direction compression, corresponding to which we denote the threshold stresses as σ_{x-SC} and σ_{y-SC}. Their variations as functions of the honeycomb prism size l are plotted in Fig. 5a and 5b. Similar to the trend of the critical elastic buckling stress (cf. Fig. 4b above), σ_{x-SC} and σ_{y-SC} decrease as l increases, and the AC honeycomb exhibits a higher σ_{x-SC} and σ_{y-SC} than the ZZ honeycomb of the same l, indicative of a better resistance to structural collapse resistance. The monotonic decline in σ_{x-SC} and σ_{y-SC} as l increases can be understood from the continuum mechanics, as to be described below. In addition, we also observed that for any graphene honeycomb, σ_{x-SC} is always smaller than σ_{y-SC}. This is due to the occurrence of junction rotation for loading in the x direction (see Section 3.1 and Fig. 2c-d), which allows large deformations of the structure at a nearly constant 'plateau' stress before structural collapse (see Fig. 2a).

Moreover, we also plotted the strains at the initiation of the structural collapse for loading in the x and y directions, denoted as ε_{x-SC} and ε_{y-SC} respectively, as functions of l in Fig. 5c and 5d. We can see that for either ε_{x-SC} or ε_{y-SC}, the data coincide into a single curve, regardless of the lattice and junction structures. This suggests that different graphene honeycombs of a particular prism size l share the same deformation limit. It also hints that the "yielding" leading to the structural collapse is occurring at bonds within the cell wall rather than those at the junction, which is indeed confirmed by further close-up examination of the atomic details of the structural evolution near the collapse event (see details in Supporting Information S1). Meanwhile, unlike the cases of elastic buckling for which the critical onset strain always revolves around 10% strain, ε_{x-SC} and ε_{y-SC} increase with the increase of l and gradually converges to steady values (being ~ 60% and ~ 80% for loading along x and y directions respectively) as l becomes rather large. Such a trend can be understood by examining the load state within the cell wall, as schematically illustrated in Fig. 5e-f. Taking the mid-point of the honeycomb cell wall as a sample point, we see that the segment OA can be approximately regarded as a cantilever beam fixed at junction O and loaded at point A by a force P. Apparently a smaller prism length l would require a larger force P to achieve the same degree of shape cell shape distortion, i.e., strain. Thus honeycomb of a smaller prism length l at a particular strain would experience higher loading, and consequently higher bending moment within the cell wall, rendering earlier structural collapse at a smaller strain.

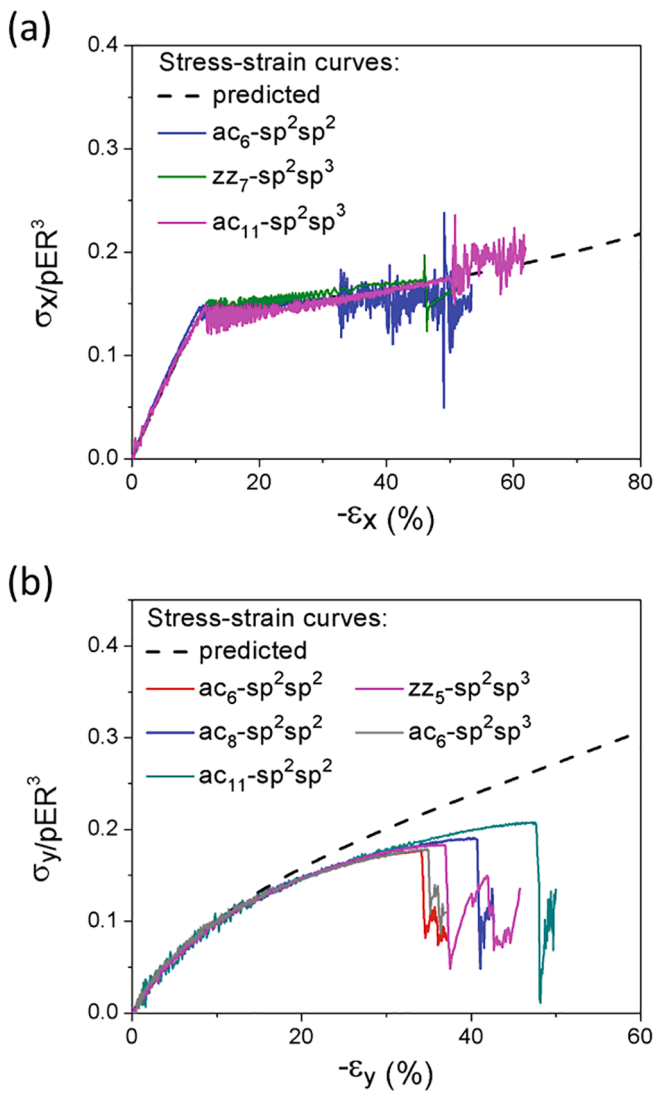

Fig. 7. (a) and (b) show the simulated stress–strain curves for graphene honeycombs loaded in $\times$ or y directions respectively, in comparison with predictions using Zhu and Mills' model and from the simulation. Note that the stress is normalized by pER^2, where p is the prefactor defined in Section 3.2, E is Young's Modulus of graphene and R is the relative density of honeycomb given by $\frac{2}{\sqrt{3}}t/l$.

As per the continuum theory, the honeycomb will collapse when the bending moment in the cell walls reaches the fully plastic moment [26]. Consequently, the structural collapse strength σ_{x-SC} and σ_{y-SC} can be predicted as:

$$\sigma_{x-SC} = \sigma_{ys}\left(\frac{t}{l}\right)^2 \frac{1}{2cos^2\theta} \tag{2}$$

and:

$$\sigma_{y-SC} = \sigma_{ys}\left(\frac{t}{l}\right)^2 \frac{1}{2\left(\frac{h}{l}+sin\theta\right)sin\theta} \tag{3}$$

where l, θ and t are the honeycomb prism size, honeycomb prism angle and the cell wall thickness previously defined in Eq. (1). In the continuum framework, σ_{ys} is defined as the yield stress of the material constituting the honeycomb, and taken as a material constant for 3D solid material. However, we can see from Fig. 6 that if σ_{ys} is treated as a constant, the model predictions from Eqs. (2) and (3) do not agree with the simulation data. In particular, the results shown in Fig. 6 seem to suggest that the honeycomb of a smaller l possess a higher σ_{ys}. The discrepancy displayed in Fig. 6 can possibly be attributed to the fact that we do not have a 3D solid material but a 2D lattice material in cell walls of the graphene honeycomb. One apparent difference resides in the process of collapse, where the 3D solid wall material fails by (e.g., shear) yielding of material, while the graphene lattice fails via abrupt local bond rotation. As mentioned earlier, the collapse occurs at bonds within the graphene cell wall but not those at the junction. Nonetheless, those bonds where the abrupt bond rotation occurs are within close vicinity to the junction, despite not immediately at the junction (see details in Supporting Information S1). As a result of this close proximity, the junction exerts some influence on the structural collapse although it does not directly participate in the process. Such influence, in a way, may be understand as constraint on rotation of those bonds within close range to the junction, which is reflected on the slight bending of local bond at the junction (see details in Supporting Information S2). The effect of constraint by the junction diminishes with the increase in the prism size, as the degree of bond bending at the junction becomes smaller (see Figure S2 in Supporting Information). In light of the above, it is reasonable to assume σ_{ys} as l-dependent rather than a constant, so as to account for the constraint exerted by the junction. Fitting the data in Fig. 5a and 5b to Eq. (2) and (3) respectively, we found that the structural collapse strength σ_{x-SC} and σ_{y-SC} can be well predicted if σ_{ys} assumes the following expression:

$$\sigma_{ys} = \sigma_{0i}^{\alpha} + \frac{k_i^{\alpha}}{l} \tag{4}$$

where σ_{0i}^{α} and k_i^{α} are two constants determined from fitting (with their values tabulated in Table S1), with αindicating the (cell nanoribbon) lattice orientation (AC or ZZ) and $i = x$ or y indicating the loading direction. The parameters σ_{0i}^{α} and k_i^{α} have dependence on the lattice orientation since junctions may exert different constraint on cell walls with different lattice structures. They also have dependence on the loading direction, because structural collapse along x and y exhibit different modes (c.f. Fig. 2), which consequently renders different modes/degrees of bond rotation involved. From Fig. 6, with the l-dependent σ_{ys} (c.f., Eq. (4)) plugged into Eq. (2) and (3), the model predictions are in excellent agreement with the simulated σ_{x-SC} and σ_{y-SC} data.

Besides those critical events, we have also devoted effects to understanding the overall deformation process, i.e., the stress-stain curve during the in-plane compression of graphene honeycombs. Adopting the model by Zhu and Mills [41], which consider the cell shape change and junction rotation during the deformation process, predictions of the overall stress–strain curves have been made (see relevant equations in Supporting Information S4). Fig. 7 compares the simulated and predicted stress–strain curves for several representative graphene honeycombs. It is important to note that in the plots, the stress is normalized by a factor pER^2, where p is the prefactor defined in Eq. (1) above (see Section 3.2), E is Young's Modulus of graphene and R is the relative density of honeycomb, defined as $\frac{2}{\sqrt{3}}t/l$ (see Supporting Information for additional details). From Fig. 7, overall we see that the model prediction correctly capture the trend and key characteristics of the stress–strain curve, despite not able to capture the event of structural collapse. Now, separately examining the two different loading directions, first, for loading along x (c.f., Fig. 7a), the predicted stress–strain relationship for honeycombs well overlaps with the simulated stress-strains curves for different graphene honeycombs at different honeycomb prism size l. Meanwhile, for honeycomb loading in the y direction, although the predicted and simulated stress–strain curves well overlap at low strains, the simulated curves give smaller stress values at high strains compared to the predicted curve (see Fig. 7b). This difference is possibly attributed to the notable effect of junction on cell wall bending, particularly at high strains. Such effect cannot be neglected for 2D lattice materials but is not accounted for in Zhu and Mills' model for regular 3D honeycombs (see

Supporting Information for additional details). Moreover, to further confirm this postulation, we have examined how the deviation between the predicted and simulated stress–strain curves varies for graphene honeycombs of different prism sizes (see Supporting Information for details). Indeed we found that the deviation amplifies as the honeycomb prism size l decreases (i.e., when a stronger junction effect is expected).

4. Conclusions

In conclusion, the deformation behaviors of 3D graphene honeycomb structures of different cell lattice orientations, cell prism sizes and junction types, under uniaxial in-plane compression, have been comprehensively studied employing large-scale molecular dynamics simulations and continuum modeling. The stress–strain responses of the graphene honeycombs were found to be dependent on the loading direction, prism size and lattice orientation, but not much affected by the junction type. Two critical deformation events, i.e., elastic buckling and structural collapse, were identified. The local and global structural changes associated with these critical events have been clarified, and the corresponding threshold stress and strain values have been obtained. In addition, the graphene honeycomb was found to exhibit a (prism) size-dependent yielding, unlike the isotropic, continuum cellular materials. Based on the continuum mechanics framework, but accounting for the effect of lattice orientation and size-dependent yielding, we have developed models able to quantitatively predict the threshold stresses for the critical deformation events of elastic buckling and structural collapse. In addition, it has been demonstrated that the overall stress–-strain curve of graphene honeycomb can also be reasonably well predicted via continuum modeling, *albeit* deviation at large strains, which can be attributed to the effect of junction on cell wall bending that is not accounted for in the continuum model. The present study provides critical mechanistic understanding and predictive tools for for optimizing and designing 3D graphene honeycombs in small-scale applications.

Declaration of Competing Interest

The authors declare that they have no known competing financial interests or personal relationships that could have appeared to influence the work reported in this paper.

Acknowledgements

The authors acknowledge financial support by the Natural Sciences and Engineering Research Council of Canada (NSERC) Discovery Grant (grant #: NSERC RGPIN-2017-05187), and the McGill Engineering Doctoral Award (MEDA). The authors also thank the Compute Canada for providing computing resources.

Data availability statement

All data generated or analysed during this study are included in this published article (and its supplementary information files).

Appendix A. Supplementary data

Supplementary data to this article can be found online at https://doi.org/10.1016/j.commatsci.2021.110646.

References

[1] S.V. Morozov, K.S. Novoselov, M.I. Katsnelson, F. Schedin, D.C. Elias, J. A. Jaszczak, A.K. Geim, Giant intrinsic carrier mobilities in graphene and its bilayer, Phys. Rev. Lett. 100 (1) (2008), 016602.
[2] A. Peigney, C.h. Laurent, E. Flahaut, R.R. Bacsa, A. Rousset, Specific surface area of carbon nanotubes and bundles of carbon nanotubes, Carbon 39 (4) (2001) 507–514.
[3] C. Lee, X. Wei, J.W. Kysar, J. Hone, Measurement of the Elastic Properties and Intrinsic Strength of Monolayer Graphene, Science 321 (5887) (2008) 385–388.
[4] K.S. Novoselov, A.K. Geim, S.V. Morozov, D. Jiang, Y. Zhang, S.V. Dubonos, I. V. Grigorieva, A.A. Firsov, Electric Field Effect in Atomically Thin Carbon Films, Science 306 (5696) (2004) 666–669.
[5] Y. Zhu, S. Murali, W. Cai, X. Li, J.W. Suk, J.R. Potts, R.S. Ruoff, Graphene and graphene oxide: synthesis, properties, and applications, Adv. Mater. 22 (35) (2010) 3906–3924.
[6] F. Scarpa, S. Adhikari, A.J. Gil, C. Remillat, The bending of single layer graphene sheets: the lattice versus continuum approach, Nanotechnology 21 (12) (2010), 125702.
[7] YongKuan Shen, HengAn Wu, Interlayer shear effect on multilayer graphene subjected to bending, Appl. Phys. Lett. 100 (10) (2012) 101909, https://doi.org/10.1063/1.3693390.
[8] S. Deng, V. Berry, Wrinkled, rippled and crumpled graphene: an overview of formation mechanism, electronic properties, and applications, Mater. Today 19 (4) (2016) 197–212.
[9] M. Li, Z. Tang, M. Leng, J. Xue, Flexible Solid-State Supercapacitor Based on Graphene-based Hybrid Films, Adv. Funct. Mater. 24 (47) (2014) 7495–7502.
[10] A.K. Geim, I.V. Grigorieva, Van der Waals heterostructures, Nature 499 (2013) 419.
[11] Y. Si, E.T. Samulski, Exfoliated Graphene Separated by Platinum Nanoparticles, Chem. Mater. 20 (21) (2008) 6792–6797.
[12] P.T. Yin, S. Shah, M. Chhowalla, K.-B. Lee, Design, Synthesis, and Characterization of Graphene-Nanoparticle Hybrid Materials for Bioapplications, Chem. Rev. 115 (7) (2015) 2483–2531.
[13] C.H. Lui, L. Liu, K.F. Mak, G.W. Flynn, T.F. Heinz, Ultraflat graphene, Nature 462 (2009) 339.
[14] M. Lanza, Y. Wang, A. Bayerl, T. Gao, M. Porti, M. Nafria, H. Liang, G. Jing, Z. Liu, Y. Zhang, Y. Tong, H. Duan, Tuning graphene morphology by substrate towards wrinkle-free devices: Experiment and simulation, J. Appl. Phys. 113 (10) (2013) 104301, https://doi.org/10.1063/1.4794521.
[15] C. Li, G. Shi, Three-dimensional graphene architectures, Nanoscale 4 (18) (2012) 5549–5563.
[16] Y. Xu, K. Sheng, C. Li, G. Shi, Self-Assembled Graphene Hydrogel via a One-Step Hydrothermal Process, ACS Nano 4 (7) (2010) 4324–4330.
[17] N.V. Krainyukova, E.N. Zubarev, Carbon Honeycomb High Capacity Storage for Gaseous and Liquid Species, Phys. Rev. Lett. 116 (5) (2016), 055501.
[18] C. Zhu, T.-Y.-J. Han, E.B. Duoss, A.M. Golobic, J.D. Kuntz, C.M. Spadaccini, M. A. Worsley, Highly compressible 3D periodic graphene aerogel microlattices, Nat. Commun. 6 (2015) 6962.
[19] Z. Chen, W. Ren, L. Gao, B. Liu, S. Pei, H.-M. Cheng, Three-dimensional flexible and conductive interconnected graphene networks grown by chemical vapour deposition, Nat. Mater. 10 (2011) 424.
[20] Q. Fang, Y. Shen, B. Chen, Synthesis, decoration and properties of three-dimensional graphene-based macrostructures: A review, Chem. Eng. J. 264 (2015) 753–771.
[21] H.R. Karfunkel, T. Dressler, New hypothetical carbon allotropes of remarkable stability estimated by MNDO solid-state SCF computations, J. Am. Chem. Soc. 114 (7) (1992) 2285–2288.
[22] X. Gu, Z. Pang, Y. Wei, R. Yang, On the influence of junction structures on the mechanical and thermal properties of carbon honeycombs, Carbon 119 (2017) 278–286.
[23] Z. Pang, X. Gu, Y. Wei, R. Yang, M.S. Dresselhaus, Bottom-up Design of Three-Dimensional Carbon-Honeycomb with Superb Specific Strength and High Thermal Conductivity, Nano Lett. 17 (1) (2017) 179–185.
[24] J. Hu, X. Zhang, Theoretical prediction of honeycomb carbon as Li-ion batteries anode material, The European Physical Journal B 91 (5) (2018) 76.
[25] L. Yi, T. Chang, X.-Q. Feng, Y. Zhang, J.i. Wang, B. Huang, Giant energy absorption capacity of graphene-based carbon honeycombs, Carbon 118 (2017) 348–357.
[26] L.J. Gibson, M.F. Ashby, Cellular solids: structure and properties, Cambridge university press1999.
[27] J. Zhang, M.F. Ashby, The out-of-plane properties of honeycombs, Int. J. Mech. Sci. 34 (6) (1992) 475–489.
[28] Z. Zhang, A. Kutana, Y. Yang, N.V. Krainyukova, E.S. Penev, B.I. Yakobson, Nanomechanics of carbon honeycomb cellular structures, Carbon 113 (2017) 26–32.
[29] F. Meng, C. Chen, D. Hu, J. Song, Deformation behaviors of three-dimensional graphene honeycombs under out-of-plane compression: Atomistic simulations and predictive modeling, J. Mech. Phys. Solids 109 (2017) 241–251.
[30] A. Kuc, G. Seifert, Hexagon-preserving carbon foams: Properties of hypothetical carbon allotropes, Physical Review B 74 (21) (2006), 214104.
[31] D. Akinwande, C.J. Brennan, J.S. Bunch, P. Egberts, J.R. Felts, H. Gao, R. Huang, J.-S. Kim, T. Li, Y. Li, K.M. Liechti, N. Lu, H.S. Park, E.J. Reed, P. Wang, B.I. Yakobson, T. Zhang, Y.-W. Zhang, Y. Zhou, Y. Zhu, A review on mechanics and mechanical properties of 2D materials—Graphene and beyond, Extreme Mechanics Letters 13(Supplement C) (2017) 42-77.
[32] N. Park, J. Ihm, Electronic structure and mechanical stability of the graphitic honeycomb lattice, Phys. Rev. B 62 (11) (2000) 7614–7618.
[33] A. Pedrielli, S. Taioli, G. Garberoglio, N.M. Pugno, Designing graphene based nanofoams with nonlinear auxetic and anisotropic mechanical properties under tension or compression, Carbon 111 (2017) 796–806.
[34] A.M. Hodge, J. Biener, L.L. Hsiung, Y.M. Wang, A.V. Hamza, J.H. Satcher, Monolithic nanocrystalline Au fabricated by the compaction of nanoscale foam, J. Mater. Res. 20 (3) (2005) 554–557.

[35] S. Plimpton, Fast Parallel Algorithms for Short-Range Molecular Dynamics, J. Comput. Phys. 117 (1) (1995) 1–19.
[36] S.J. Stuart, A.B. Tutein, J.A. Harrison, A reactive potential for hydrocarbons with intermolecular interactions, J. Chem. Phys. 112 (14) (2000) 6472–6486.
[37] T. Zhang, X. Li, H. Gao, Designing graphene structures with controlled distributions of topological defects: A case study of toughness enhancement in graphene ruga, Extreme Mech. Lett. 1 (2014) 3–8.
[38] T. Zhang, X. Li, S. Kadkhodaei, H. Gao, Flaw Insensitive Fracture in Nanocrystalline Graphene, Nano Lett. 12 (9) (2012) 4605–4610.
[39] H. Zhao, K. Min, N.R. Aluru, Size and Chirality Dependent Elastic Properties of Graphene Nanoribbons under Uniaxial Tension, Nano Lett. 9 (8) (2009) 3012–3015.
[40] C. Combescure, P. Henry, R.S. Elliott, Post-bifurcation and stability of a finitely strained hexagonal honeycomb subjected to equi-biaxial in-plane loading, Int. J. Solids Struct. 88-89 (2016) 296–318.
[41] H.X. Zhu, N.J. Mills, The in-plane non-linear compression of regular honeycombs, Int. J. Solids Struct. 37 (13) (2000) 1931–1949.
[42] L. Cao, F. Fan, Deformation and instability of three-dimensional graphene honeycombs under in-plane compression: Atomistic simulations, Extreme Mech. Lett. 39 (2020) 100861, https://doi.org/10.1016/j.eml.2020.100861.
[43] Q. Zheng, Y. Geng, S. Wang, Z. Li, J.-K. Kim, Effects of functional groups on the mechanical and wrinkling properties of graphene sheets, Carbon 48 (15) (2010) 4315–4322.
[44] B.I. Yakobson, C.J. Brabec, J. Bernholc, Nanomechanics of Carbon Tubes: Instabilities beyond Linear Response, Phys. Rev. Lett. 76 (14) (1996) 2511–2514.